Nanoscale

PAPER

View Article Online
View Journal | View Issue

Cite this: *Nanoscale*, 2018, **10**, 10203

Boron-doped graphene nanosheet-supported Pt: a highly active and selective catalyst for low temperature H_2-SCR†

Maocong Hu,[a] Zhenhua Yao,[a] Lili Li,[b] Yung-Hao Tsou,[a] Liyuan Kuang,[c] Xiaoyang Xu,[a] Wen Zhang[c] and Xianqin Wang*[a]

Received 3rd March 2018,
Accepted 30th April 2018

DOI: 10.1039/c8nr01807c

rsc.li/nanoscale

A series of boron-doped graphene-supported Pt (Pt/BG) nanosheets were designed and synthesized using a one-step facile hydrothermal method. ICP, XPS, and TPD results confirmed that boron atoms were successfully embedded into the graphene matrix. The selective catalytic reduction of nitric oxide with hydrogen (H_2-SCR) was tested over Pt/BG catalysts. The multi-roles of doped-boron were investigated by Raman, BET, CO-chemisorption, H_2-TPD, XPS, and NO-TPD. Boron doping led to a higher dispersion and smaller size of Pt nanoparticles, facilitated hydrogen spillover, promoted more metallic Pt formation, and increased both H_2 and NO chemisorption, which were attributed to an enhanced Pt nucleation rate over doped-boron, electron donation from boron to Pt, and extra chemisorption sites. The reaction performances (conversion 94.7%, selectivity 90.3%, and TOF 0.092 s^{-1}) were greatly promoted attributing to a bifunctional catalytic mechanism. This work paves the way to modify the structure and tune the chemisorption ability of graphene-based catalysts, and provides novel insights for designing high performance catalysts.

1. Introduction

Selective catalytic reduction of nitric oxide with hydrogen (H_2-SCR), introduced by Jones *et al.* in the 1970s,[1] can be used for both stationary sources like power plants and mobile applications.[2–4] H_2-SCR is an attractive approach for NO_x removal at low temperatures (T < 200 °C) with high activity[5,6] while the widely studied NH_3-SCR, selective catalytic reduction of NO_x by ammonia, works in a temperature range of 200–500 °C[6–13] and the NO_x removal activity of the developing HC-SCR, selective catalytic reduction of NO_x by hydrocarbons, is still in early development for practical applications below 200 °C.[14–16] Moreover, H_2-SCR is considered as a more promising approach than NH_3-SCR or HC-SCR in some specific applications, such as cold start conditions or lean-burn diesel engines, where the exhaust temperature has become lower and lower for improving engine thermal efficiency.[17]

To date, supported noble metal catalysts are the most widely investigated catalysts for H_2-SCR[18–20] while platinum (Pt) based catalysts are reported to be the most active.[21–23] Pt catalysts supported on various supports, such as Pt/WO_3–TiO_2,[24] Pt/Al_2O_3,[25,26] Pt/SiO_2,[27] Pt/TiO_2–ZrO_2,[28] Pt/MgO–CeO_2,[29] Pt_1/FeO_x,[30] Pt/H-ferrierite (H-FER),[31] Pt/$NiFe_2O_4$,[32] Pt/microporous zeolites (*i.e.* MFI, MOR, beta, and Y),[33,34] Pt/HZSM-5,[35] Pt/ZSM-35[36] and Pt-ZSM-5,[37] and Pt supported on oxidic/perovskitic solid materials,[38,39] were proposed and it was suggested that the basicity of supports has a negative effect on the activity while supports with solid acidity generally show good catalytic performance since acid sites could facilitate NH_4^+ storage leading to selective N_2 formation through a well-established NH_3-SCR mechanism.[17,33,34] The oxidation states and dispersion of Pt are the other two key factors controlling H_2-SCR activity.[3,17] It is believed that metallic Pt (Pt^0) is the active site during the SCR process while $Pt^{II}O$ and $Pt^{IV}O_2$ are inactive for de-NO_x due to the coverage of O_{ad} and the formation of the oxidation state.[16,40,41] Moreover, a correlation of Pt dispersion with the specific rate of H_2-SCR was observed and the reaction rate dropped by more than one order of magnitude when the Pt dispersion decreased from 90% to 10%.[29] Therefore, a high dispersion of metallic Pt supported on an acidic support is regarded as a promising alternative strategy to improve the reaction performance of H_2-SCR.[3,17]

Graphene, the two-dimensional allotrope of carbon, has attracted much attention as a catalyst support because of its

[a]*Department of Chemical and Materials Engineering, New Jersey Institute of Technology, Newark, NJ 07102, USA. E-mail: xianqin.wang@njit.edu; Fax: +1 973 596 8436; Tel: +1 973 596 5707*
[b]*Department of Life Science, Zhoukou Normal University, Zhoukou 466000, China*
[c]*John A. Reif, Jr. Department of Civil and Environmental Engineering, New Jersey Institute of Technology, Newark, New Jersey 07102, USA*
†Electronic supplementary information (ESI) available. See DOI: 10.1039/c8nr01807c

unique structure, superior stability, and large surface area.[42–44] Moreover, the high-efficiency process of gain and loss of electrons due to the excellent electron mobility of graphene leads to improved redox performance and catalytic reduction ability of catalysts. Recently, graphene based metal oxides such as reduced graphene oxide supported Mn_2CoO_4,[45] TiO_2-graphene supported MnO_x,[46] TiO_2-graphene supported CeO_x–MnO_x,[47] and graphene supported MnO_x–CeO_2[48] were investigated for NH_3-SCR and displayed enhanced activities, which were attributed to high specific surface areas and excellent redox performance. However, uniformly anchoring catalytically active species on pristine graphene is difficult due to its perfect graphitization, low defect level and smooth surface, which may reduce the catalytic activity of the supported catalyst nanoparticles towards the desired reaction.[49,50] Heteroatom doping is an effective approach to produce a large number of defect sites in the basal planes and edges of graphene sheets, which can serve as loading sites for anchoring metal nanoparticles.[51] Boron atoms, with comparable atomic size and three valence electrons for binding with carbon atoms, could be incorporated into the carbon matrix.[52,53] In previous several years, boron doped graphene (BG) based catalysts have been widely studied and mainly used in oxygen reduction reactions for fuel cells.[54] However, to the best of our knowledge, no study using doped graphene as a support for H_2-SCR catalysts has been reported. Furthermore, boron has a lower electronegativity than carbon and Pt, and therefore, boron would donate an electron to carbon and Pt.[49,55] Therefore, p-type (or hole) doped graphene would be produced leading to more acid sites and metallic Pt formation. Thus, it suggests us to explore the potential applications of Pt/BG for the H_2-SCR reaction. Moreover, a comprehensive understanding of the role of doped-boron in Pt/BG catalysts and overall catalytic activity for the H_2-SCR process is important for designing and preparing H_2-SCR catalysts with tailorable catalytic properties.

In this work, a series of Pt/BG catalysts were prepared by a hydrothermal method. The multi-roles of doped-boron in the structure of the graphene matrix, dispersion and size of Pt nanoparticles, chemisorption ability to nitric oxide and hydrogen, and the overall reaction performance of H_2-SCR were systematically investigated using inductively coupled plasma-mass spectroscopy (ICP-MS), X-ray photoelectron spectroscopy (XPS), Raman spectroscopy, Brunauer–Emmett–Teller (BET), CO-chemisorption, Temperature Programmed Decomposition (TPD), hydrogen-Temperature Programmed Desorption (H_2-TPD), nitric oxide-Temperature Programmed Desorption (NO-TPD), and a kinetic study.

2. Experimental

2.1. Pt/boron-doped graphene preparation

Pt/boron-doped graphene (Pt/BG) catalysts were prepared by a one-pot hydrothermal method using homemade graphene oxide (GO) as the substrate while $Pt(NH_3)_4(NO_3)_2$ (Strem Chemicals) and boric acid (ACROS Organics) were the Pt and boron sources, respectively. GO was synthesized from natural graphite powder (Alfa Aesar) based on a modified Hummers' method.[42,56] A typical synthesis of the Pt/BG catalyst was carried out as follows: 80 mL of prepared GO dispersion (containing 0.2 g carbon) was sonicated for 1 h to produce GO nanosheets. About 15 mL of boric acid solution was added dropwise to the above dispersion with vigorous stirring for 0.5 h. The concentration of boric acid solution was determined by the different weight ratios of boron/(boron + carbon) (0, 10, 20, 30%). 5 ml $Pt(NH_3)_4(NO_3)_2$ solution (with a nominal Pt weight ratio of 1%) was then added to the mixture dropwise with vigorous stirring for 0.5 h. Finally, the above mixture was transferred into a Teflon-lined stainless-steel autoclave with a capacity of 200 mL for hydrothermal treatment at 180 °C for 16 h. The autoclave was then left to cool down to room temperature. The precipitate was separated by centrifugation, washed with distilled water and ethanol three times, and dried at 60 °C overnight. The samples were labeled as Pt/Gr (Pt/graphene, no boron doping), Pt/BG10, Pt/BG20, and Pt/BG30 based on the boron weight ratio. For comparison, boron-doped graphene (with a boron ratio of 20%) was prepared under the same hydrothermal conditions without $Pt(NH_3)_4(NO_3)_2$ and labeled as BG20.

2.2. Pt/BG characterization

Elemental analysis of the samples was carried out by ICP-MS (Agilent, 7700X). XPS measurements were performed on a Kratos Axis Ultra DLD multi-technique X-ray photoelectron spectroscope. The binding energy for all samples was calibrated by the reference C 1s binding energy (284.8 eV). Raman spectroscopy was performed with a Thermo Scientific DXR Raman microscope. The specific surface area of the reduced sample was determined by N_2 adsorption/desorption at liquid nitrogen temperature using an AutoChem 2920 II (Micromeritics). TPD was carried out using a Micromeritics AutoChem II 2920 system. Samples were heated in flowing helium from room temperature to 1000 °C at a heating rate of 10 °C min^{-1}. The effluent gas was analyzed with an on-line mass spectrometer (QMS 200, Stanford Research Systems). Hydrogen and nitric oxide TPD (H_2- and NO-TPD) was carried out using the same apparatus described previously. Catalysts were preheated at 180 °C for 1 h and exposed to H_2 or NO until the sample was saturated before heating to 750 °C at a heating rate of 10 °C min^{-1} in a helium flow of 50 mL min^{-1}. Possible residual gases including H_2, NO, N_2O, and N_2 were monitored. CO chemisorption was measured by using an AutoChem 2920 II (Micromeritics) equipped with a thermal conductivity detector (TCD).

2.3. Reaction performance testing

The selective catalytic reduction of NO by hydrogen at atmospheric pressure was performed in a continuous fixed-bed reactor. The typical reactants were NO (1000 ppm), H_2 (5000 ppm), and O_2 (6%) balanced with He and the total flow rate was 200 ml min^{-1}, and the GHSV was about 80 000 h^{-1}. Granular Pt/BG catalysts (~100 mg) were stabilized on quartz

wool which was supported by SiC (40–60 mesh average grain size, Alfa Aesar). The products were analyzed with an on-line mass spectrometer (QMS 200, Stanford Research Systems).[38,39,57] The MS signals were converted to gas concentrations by a pre-determined calibration curve. All of the reaction data were collected when the reaction reached a steady state. N-Containing product species produced in the present catalytic reaction system were N_2 and N_2O. The nitrogen balance was calculated for each step using the following equation: $[NO]_{in} = [NO]_{out} + 2[N_2O] + 2[N_2]$, where $[NO]_{in}$ is the NO molar flow rate in the feed, and $[NO]_{out}$, $[N_2O]$, and $[N_2]$ are the NO, N_2O, and N_2 molar flow rates in the effluent stream, respectively. The N-balance was found to be >95% for all the experiments. NO_x conversion and N_2 selectivity were calculated based on eqn (1) and (2), respectively. The TOF of the samples was calculated using eqn (3). NO consumption rates were obtained using a differential reactor with NO conversion below 20% and calculated by eqn (4), where r_{NO}, C_{in}, v, X, and W are the reaction rates of NO, NO concentration in feed, total molar flow rate, NO conversion, and catalyst weight, respectively.

$$X = \frac{[NO]_{in} - [NO]_{out}}{[NO]_{in}} \times 100\% \quad (1)$$

$$S_{N_2} = \frac{2\,[N_2]}{[NO]_{in} - [NO]_{out}} \times 100\% \quad (2)$$

$$TOF = \frac{[NO]_{in} - [NO]_{out}}{\text{Number of surface sites}} \quad (3)$$

$$r_{NO} = \frac{C_{in} v X}{W} \quad (4)$$

3. Results and discussion

3.1. Embedding boron into graphene matrix

The desired catalyst in this work is the boron-doped graphene supported platinum, which was synthesized by a one-pot hydrothermal method instead of an annealing approach or CVD synthesis under harsh conditions.[58] The bulk and surface compositions of the synthesized samples were first investigated by ICP and XPS, respectively, to confirm the boron doping into the graphene matrix and the results are shown in Table 1. The boron contents in bulk, the mass of boron to the total mass of the sample, were determined to be 0.037–0.056% over different samples, suggesting that boron species are present in the prepared catalysts. Boron loadings in the surface were around 10–15 times (0.42–0.64%) higher than those in the bulk as measured by XPS, indicating that most of the boron atoms were located on the surface after the hydrothermal process. In this work, multi-layer graphene (confirmed in the next section) instead of the single-layer one was employed as the catalyst support. Accordingly, there are outer- and inter-layer surfaces, respectively. It would be much easier for the boron atoms embedding into the outer-graphene matrix than those into the inner matrix. Pt loadings in the bulk were determined to be more than 0.9% for all samples, which is close to the nominal percentage (1%). However, the Pt content on the surface was lower than that in the bulk because some Pt atoms deposited on the graphene sheet and further wrapped by multi-layer graphene during the hydrothermal process, which is out of the limited penetration depth by the XPS.[59]

To confirm that the surface boron atoms are embedded into the graphene matrix and are not simply accumulating on the surface, the high-resolution XPS spectra of B 1s, C 1s and O 1s were collected and are shown in Fig. 1 (using Pt/BG20 as an example). B 1s binding energy (192.2 eV) is higher than that of pure boron (187.0 eV) and lower than that of boron oxide (193.7 eV), indicating that boron atoms are bound to carbon atoms in the sp^2-C network.[51] The incorporation of boron can disrupt the sp^2 hybridization of carbon atoms. Furthermore, the B 1s peak can be deconvoluted into two peaks at 192.05 eV and 192.35 eV, which are assigned to BC_2O and BCO_2, respectively, two typical bonds in boron-doped graphene. Compared to Pt/Gr, two new peaks were observed on the C 1s spectrum of Pt/BG20, which can be assigned to $C–B_1$ and $C–B_2$ respectively,[60,61] indicating that boron atoms were bonded to carbon atoms in two ways, which is consistent with the results of B 1s.

Table 1 Bulk and surface composition of different samples

	Bulk composition determined by ICP-MS		Surface composition measured by XPS	
Sample	Boron (wt%)	Pt (wt%)	Boron (wt%)	Pt (wt%)
Pt/Gr	—	0.95	—	0.61
Pt/BG10	0.037	0.91	0.42	0.73
Pt/BG20	0.056	0.90	0.64	0.78
Pt/BG30	0.044	0.94	0.51	0.71
BG20	0.052	—	0.63	—

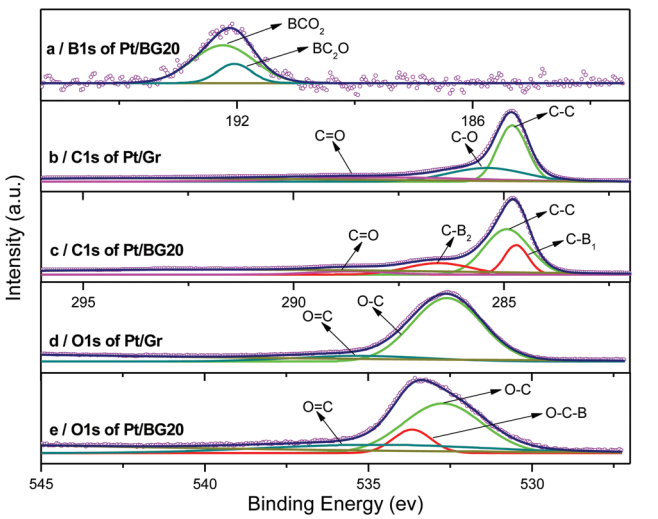

Fig. 1 B 1s (a), C 1s (b, c) and O 1s (d, e) XPS spectra of Pt/graphene (Pt/Gr) and Pt/boron-doped graphene (Pt/BG20).

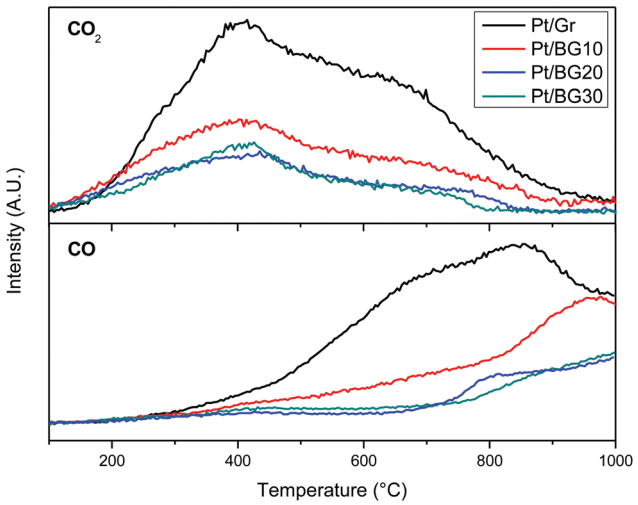

Fig. 2 CO_2 and CO profiles of TPD over different samples. The data have been normalized by sample weight.

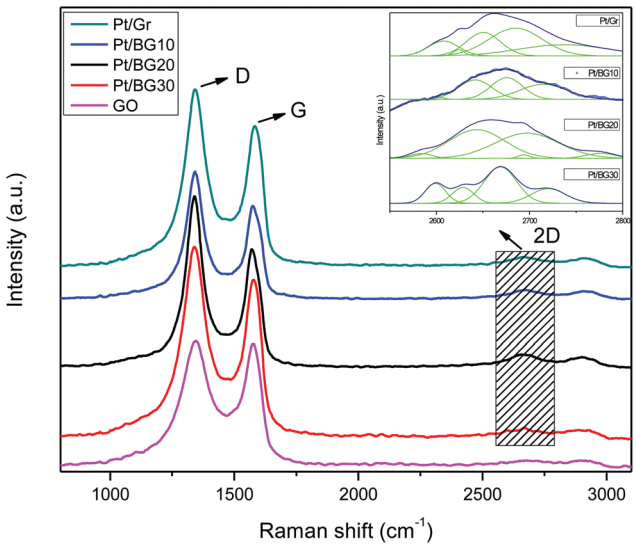

Fig. 3 Raman spectra of different samples. Inset: Fitting of 2D peaks.

Moreover, the ratio of C–C is decreased considerably from 54.72% for Pt/Gr to 47.95% for Pt/BG20, which results from the boron replacement of carbon in the graphene matrix. The new peak centered at 533.65 eV in the deconvoluted O 1s spectra, which can be ascribed to an O–C–B bond,[62] further confirmed the embedment of boron into the graphene matrix.

To further understand the boron incorporation mechanism, TPD was carried out over different samples and the results are shown in Fig. 2. The graphene or reduced graphene oxide (rGO) synthesized by a hydrothermal method contained lots of residual oxygen functional groups such as carboxyl, hydroxyl, epoxy, carbonyl, anhydride and aldehydes, which would release CO_2 and CO during TPD. The most intensive evolution of CO_2 and CO was observed over the undoped sample, Pt/Gr. Less CO_2 and CO were released with boron incorporation, indicating that less amounts of surface oxygen groups were in boron-doped samples, which may be attributed to the partial replacement of oxygen atoms by boron atoms.[63] The ICP-MS, XPS (B 1s, C 1s and O 1s), and TPD results confirmed that boron successfully embedded into the graphene matrix by replacing both carbon and oxygen atoms of graphene oxide with a hydrothermal process.

3.2. Roles of boron in catalysts' structure and chemisorption ability

Raman spectroscopy was conducted to investigate the effect of boron embedment on the stack structure and the hybridization conditions of graphene. The results are demonstrated in Fig. 3. The data of graphene oxide (GO) were also added as a reference. Two characteristic peaks, D-band (1342 cm^{-1}) and G-band (1584 cm^{-1}), were observed on all samples. The D-band (disordered band) was attributed to the breathing mode of the sp^2 rings of the graphene layer from the sp^3 defect sites while the G band was attributed to the E_{2g} phonon of the sp^2-bonded carbon atoms in a two-dimensional hexagonal lattice. The intensity ratio between the D and G peaks (I_D/I_G) is widely used to reflect the defect level in graphene.[64] The I_D/I_G ratios of different samples are listed in the first column of Table 2. Compared to GO (1.03), Pt/Gr and Pt/BG10-30 samples had a larger I_D/I_G value (1.26–1.46), clearly indicating an increase in sp^3 defect sites, which is due to the complicated reduction process occurring on the surface of the graphene sheet during hydrothermal treatment.[42] The increase in the I_D/I_G ratio with the increase in boron addition was also observed, which can be ascribed to the boron doping. The I_D/I_G ratio did not increase with higher B-doping levels (Pt/BG20 and Pt/BG30 had the same I_D/I_G ratio of 1.46), suggesting that most of the B-doping should have been either BC_2O or BCO_2 type,[65] which is consistent with the B 1s and C 1s XPS results. Furthermore, the deconvolution of 2D is given in the inset of Fig. 3, which can be used to determine the layer number of graphene.[66,67] After peak fitting, the difference in the Raman shift of the two dominant subcomponents of the 2D band ($\Delta\nu$) was found to increase with the increase in boron doping (the second column of Table 2), corresponding to the increase in the number of graphene layers. The layer number of Pt/Gr can be determined to be ~5 layers based on the $\Delta\nu$ value (28.4 cm^{-1}) comparable to that of the literature (28 cm^{-1})[66] while those of Pt/BG10, 20 and 30 are more than 5 layers. The detailed reasons for the different layers obtained on the samples will be discussed in the following sections.

BET surface area data of different samples are listed in the third column of Table 2. Theoretical calculations indicated that the highest surface area of a single layer graphene is 2630 $m^2\ g^{-1}$. Due to the random agglomeration and overlap of exfoliated graphene sheets, the actual area of graphene-based catalysts is usually much lower than that value. Boron-doped graphene (BG20) has a BET surface area of 59.6 $m^2\ g^{-1}$ which could be due to the aggregation of the graphene layers during the hydrothermal process. The BET surface area of Pt/Gr is

Table 2 Parameters derived from Raman, BET, CO-chemisorption, and Pt 4f XPS spectral measurements

	Raman			CO-chemisorption			Pt 4f XPS spectra (%)		
Sample	I_D/I_G	$\Delta\nu$ (cm^{-1})	BET ($m^2\ g^{-1}$)	CO uptake ($\mu mol\ g^{-1}$)	Pt dispersion (%)	Pt size (nm)	Pt^0	Pt^{II}	Pt^{IV}
Pt/Gr	1.26	28.4	210.5	12.8	26.2	4.32	35.7	48.5	15.8
Pt/BG10	1.37	31.6	150.6	16.9	36.4	3.11	50.1	7.4	42.5
Pt/BG20	1.46	54.1	111.1	21.1	45.7	2.48	59.8	40.2	0
Pt/BG30	1.46	71.3	92.1	22.9	47.8	2.37	52.6	37.9	9.5
GO	1.03	—	—	—	—	—	—	—	—
BG20	—	—	59.6	—	—	—	—	—	—

210.5 $m^2\ g^{-1}$, which is more than three times larger than that of BG20. The result suggests that relatively huge Pt nanoparticles were dispersed on the graphene surface among the layers, which helped to prevent restacking of the graphene sheets as nanospacers and resulted in a surface area increase. The BET surface areas of Pt supported doped-graphene samples, Pt/BG10, 20, and 30, were 150.6, 111.1, and 92.1 $m^2\ g^{-1}$, respectively. The results are consistent with the Raman 2D deconvolution results that the layer number increased with the increase in boron. Studies showed that obtaining a uniform size distribution depends on competing nucleation and growth. Instantaneous nucleation leads to homogeneous particle growth while progressive nucleation leads to heterogeneous particle growth.[68] Moreover, the nucleation rate would be enhanced over heteroatom doped sites.[69] In the graphene network of Pt/BG10, 20, and 30, doped boron created more defect sites and served as anchoring sites for Pt nanoparticles, which led to instantaneous nucleation and prevention of agglomeration of the Pt particles and further improved Pt dispersion compared to Pt/Gr. This hypothesis was further confirmed by the CO-chemisorption results as shown in Table 2. With boron doping, the exposed Pt (*i.e.*, CO uptake) increased from 12.8 to 22.9 $\mu mol\ g^{-1}$, leading to an increase in the dispersion of Pt from 26.2% to 47.8% and thus the size of the Pt nanoparticle decreased from 4.32 to 2.37 nm.

To further investigate Pt dispersion on boron-doped graphene, H_2-TPD was carried out and the profiles are demonstrated in Fig. 4. The signal from BG20 was too low to be discriminated as a peak indicating the poor chemisorption ability of doped-graphene for hydrogen. The peak area of the other four samples followed the order Pt/Gr < Pt/BG10 < Pt/BG20 < Pt/BG30, originating from the superior chemisorption ability of Pt. The observed trend is attributed to the increased number of exposed Pt (Pt dispersion), which is consistent with the findings of the above CO-chemisorption measurements. Moreover, hydrogen spillover (peak at 566 °C) was noticeable on the boron-doped samples (Pt/BG10, 20, and 30) with the maximum on Pt/BG20. Metal dispersion is the crucially important factor for hydrogen spillover storage on metal/carbon materials. For Pt on carbon (Pt/C), dispersion into nearly 2 nm clusters or nanoparticles is necessary to facilitate spillover.[70] The difference in the hydrogen spillover between the undoped and doped graphene supported samples further confirmed the increased Pt dispersion with boron doping in the graphene

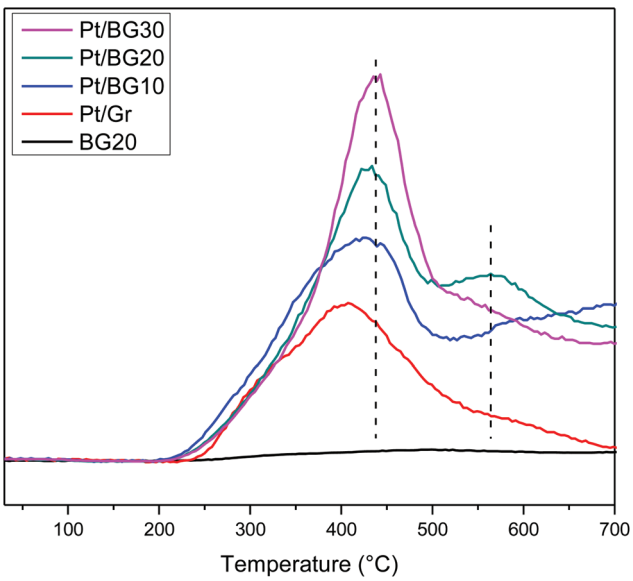

Fig. 4 H_2-TPD profiles over different samples. The data have been normalized by sample weight.

matrix. Therefore, it may be concluded that with boron incorporation into the graphene matrix the dispersion of the supported Pt nanoparticles was enhanced while the particle size decreased compared to that on the undoped graphene support.

The influence of boron doping on metallic Pt (Pt^0) formation was revealed by the high-resolution XPS spectra of Pt 4f as shown in Fig. 5. Pt^0 is considered as the active site during the SCR process while $Pt^{II}O$ and $Pt^{IV}O_2$ are inactive for de-NO_x due to the coverage of O_{ad} and the formation of the oxidation state.[16,40,41] Five peaks were observed on Pt/Gr (without boron doping) after fitting, which can be ascribed to Pt^0 at 74.9 and 71.4 eV, Pt^{II} at 75.9 and 72.05 eV, and Pt^{IV} at 72.9 eV, respectively.[41,71] On boron-doped graphene (samples Pt/BG10, 20, and 30), Pt with different valences also existed based on the deconvolution results. However, the valence distribution of Pt species in different samples dramatically changed, which is summarized in the last three columns of Table 2. For Pt/Gr, only 35.7% surface Pt species is Pt^0 while it accounts for more than 50% on the three boron-doped samples. Particularly, Pt/BG20 possessed nearly 60% metallic Pt. The increased Pt^0

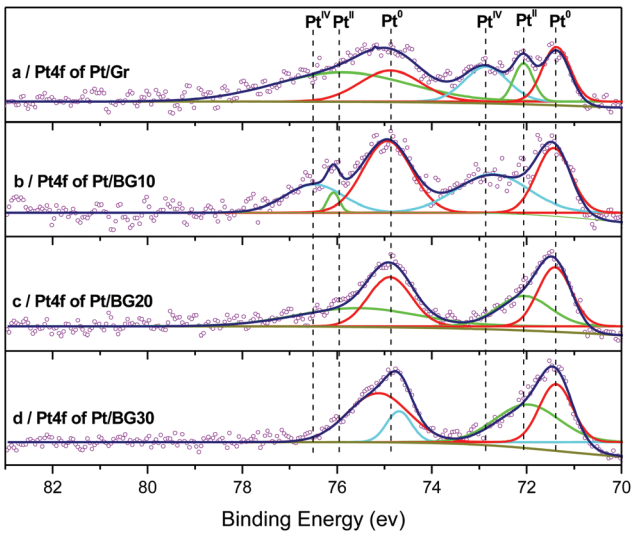

Fig. 5 Pt 4f XPS spectra of different samples. Small, open circles in purple are the measured experiment points. Curves in red, green, and cyan represent Pt^0, Pt^{II}, and Pt^{IV}, respectively. The solid line in navy is the sum of all the peak fittings.

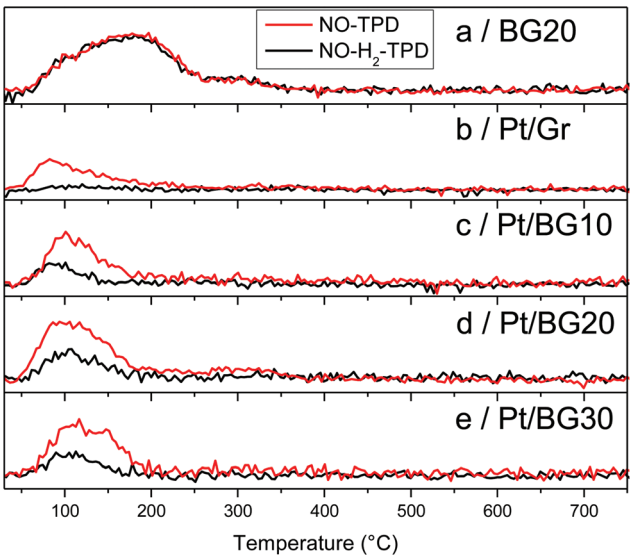

Fig. 6 NO profiles of NO-TPD and NO-H_2-TPD over different samples. The data have been normalized by sample weight. The *Y*-axes of the five panels are on the same scale.

content after boron doping can be attributed to the Pt–boron electron-interaction. With the introduction of boron species, due to the lower electronegativity of boron than Pt, boron would donate electrons to Pt. As a result, the Pt species may be reduced by the donated electrons to some extent, supporting a corresponding relationship between the surface boron loading and metallic Pt content (the fourth column of Table 1 and the eighth column of Table 2). Both had the same order Pt/BG10 < Pt/BG30 < Pt/BG20. Pt/BG20 had the maximum surface boron, leading to the highest metallic Pt content.

The effect of doped-boron on the catalyst acidity was evaluated by NO chemisorption. Two types of measurements were performed, NO-TPD (without H_2 pre-adsorption) and NO-H_2-TPD (with H_2 pre-adsorption). The NO-TPD followed the normal procedure of TPD while the NO-H_2-TPD has a pre-adsorption of hydrogen until saturation before NO adsorption. The desorbed NO profiles are demonstrated in Fig. 6 and the amounts of desorbed NO are listed in Table 3. The NO desorption amount (μmol per gram of sample) was calculated by the integration of the peak areas from TPD profiles and calibrated with the integrated areas from a known amount of NO.

NO-TPD results from BG20 (boron-doped graphene, red line in the top panel of Fig. 6) revealed that strong affinity existed between BG20 and NO. Since graphene didn't exhibit any chemisorption ability to NO (not shown here), the adsorbed NO should be related to doped-boron moieties. This result is consistent with the findings of Kawai *et al.*:[72] boron-doped graphene showed high acidity to enhance NO (a base) chemisorption; non-dissociate adsorption of the NO molecule was bound to the B site *via* the N atom, which was confirmed by simulated scanning tunneling microscopy (STM) image with an optimized adsorption model in their study. NO-H_2-TPD of BG20 (black line) gave almost the same NO profile with NO-TPD,

Table 3 Amount of NO desorption detected during two kinds of TPD and TOF of different catalysts for H_2-SCR reaction

Sample	NO-TPD (Pt + B sites, μmol g^{-1})	NO-H_2-TPD (B sites, μmol g^{-1})	Difference (Pt sites, μmol g^{-1})	TOF (s^{-1})[a]
BG20	48.6	48.6	0	—
Pt/Gr	10.9	0	10.9	0.066
Pt/BG10	22.3	9.5	12.8	0.080
Pt/BG20	30.8	11.3	19.5	0.092
Pt/BG30	30.6	9.1	21.5	0.087

[a] Calculated at 105 °C under kinetics controlled regime.

indicating that no site was occupied by hydrogen, which is consistent with the H_2-TPD results that BG20 showed no affinity to hydrogen (Fig. 4). Pt/Gr also demonstrated chemisorption ability to NO based on the NO-TPD results, which is attributed to Pt sites. However, no peak was observed in NO-H_2-TPD of Pt/Gr, suggesting that pre-adsorbed hydrogen occupied all the Pt active sites. With the NO-TPD and NO-H_2-TPD results of BG20 and Pt/Gr, we conclude that NO can be adsorbed by both doped-boron moieties over the B site *via* the N atom and Pt sites while hydrogen is only bound to Pt sites. Therefore, the desorbed NO from Pt/BG10, 20, and 30 (Pt/boron-doped graphene) consisted of two parts: NO adsorption on B sites (black line in Fig. 6) and Pt sites (the difference between the red and black line). As shown in Table 3, the amounts of NO adsorption on Pt + B sites on Pt/BG10, 20, and 30 (22.3, 30.8, and 30.6 μmol g^{-1}) are lower than that of BG20 (48.6 μmol g^{-1}) probably due to the partial coverage of doped-boron sites by Pt, while they are higher than that of Pt/Gr (10.9 μmol g^{-1}) attributing to the extra B sites introduced by boron doping. Moreover, the decreased active B sites of Pt/

BG10, 20, and 30 (the third column of Table 3) compared to BG20 further confirmed the partial coverage of B sites by Pt nanoparticles. Pt/BG20 had the most active B sites for NO adsorption (11.3 μmol g^{-1}) while Pt/BG10 and 30 possessed similar amounts (9.5 and 9.1 μmol g^{-1}). The derived amounts of Pt sites (the fourth column of Table 3) had the same trend, Pt/Gr < Pt/BG10 < Pt/BG20 < Pt/BG30, as determined in CO-chemisorption. Therefore, it can be concluded that boron doping introduced extra adsorption sites (besides Pt sites) for NO while the hydrogen adsorption still stayed on Pt sites, which allowed the bifunctional catalysis to take place on the Pt/boron–graphene catalysts.

3.3. Reaction performance

No reaction was observed on BG20 because it had no adsorbed hydrogen though it showed great chemisorption ability to NO. The reaction performance over different Pt catalysts (with and without boron doping) is summarized in Fig. 7. Generally, the conversion over all catalysts showed a typical volcano curve which can be attributed to the competitive reaction of NO and O_2 with H_2. At low temperature, the dominant reaction was the reduction of NO with H_2 while the combustion of H_2 became the primary reaction at high temperature (confirmed by water produced and H_2 consumed profiles in ESI, Fig. S1 and S2†). It is seen that the boron doping has a great effect on the activity of Pt catalysts. At the same temperature, Pt/BG20, Pt/BG30, and Pt/BG10 showed higher activity than Pt/Gr, which may be attributed to the superior chemisorption ability to H_2 and NO from the higher dispersed Pt, more metallic Pt, and extra active sites existing in these B-doped catalysts.

More importantly, the optimal operation temperature (at the highest conversion) decreased apparently with boron doping. The optimal temperature for Pt/Gr was 150 °C (conversion, 60.9%), while the optimal temperatures for Pt/BG20 (94.7%), Pt/BG30 (93.2%), and Pt/BG10 (85.8%) were 105 °C, 105 °C and 120 °C, respectively. It may be related to the higher Pt dispersion to lower the activation energy of the reaction. To test this assumption, the kinetic experiments were performed and the Arrhenius plots of H_2-SCR over different catalysts are demonstrated in Fig. 8. The apparent activation energies (E_a) of Pt/Gr, Pt/BG10, 20, and 30 were determined to be 37.6 ± 0.5, 33.1 ± 0.9, 29.4 ± 0.5, and 30.6 ± 0.5 kJ mol^{-1}, respectively, which are close to the value achieved on Pt/TiO_2 with (33 kJ mol^{-1}) and without (38 kJ mol^{-1}) WO_3 for H_2-SCR.[24] It is evident that the E_a over catalysts with boron doping are lower than that of the undoped catalyst, suggesting that the H_2-SCR of NO_x proceeds more easily due to boron doping. TOFs of different catalysts were also calculated at 105 °C under a kinetic controlled regime and are listed in the last column of Table 3. Apparently, the catalysts with boron doping had higher TOFs than the undoped ones. The highest TOF was achieved on Pt/BG20 (0.092 s^{-1}) which is almost 50% higher than that of Pt/Gr (0.066 s^{-1}). In summary, it can be concluded that boron doping greatly promoted the activity and efficiency of Pt/graphene for H_2-SCR.

In this work, two types of N-containing products were detected: N_2 as the targeted product and N_2O as an undesired by-product. N_2 selectivity dependence on temperature over different catalysts is shown in the lower panel of Fig. 7. The selectivity increased with increasing reaction temperature because NO dissociation on Pt was facilitated as the temperature was increased, thus favoring N_2 formation.[73] It can be seen that Pt/Gr held a relatively high selectivity for N_2 in H_2-SCR. Moreover, the selectivity was improved after boron doping, and the highest selectivity was achieved on Pt/BG20 (90.3% at the temperature as the conversion achieved at the maximal, *i.e.*, 105 °C). It can be attributed to three beneficial effects from boron doping: more metallic Pt formation, extra active sites of B for NO adsorption, and increased acidity of the catalyst. It is believed that N_2O is produced by neighboring NO_{ad} and O_{ad}.[3] The more metallic Pt led to reduced adsorbed

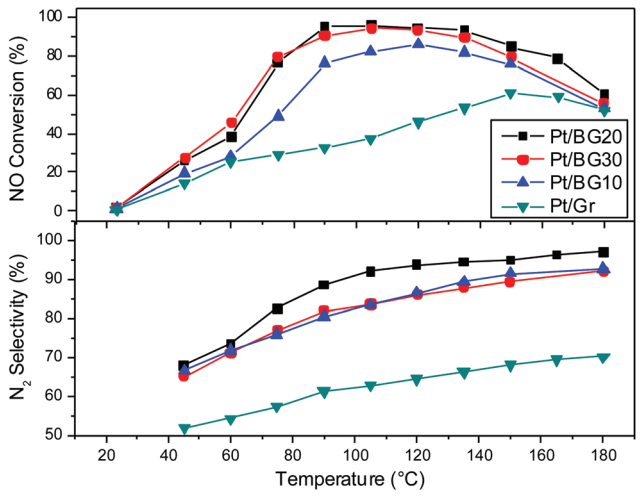

Fig. 7 Reaction performance of different catalysts for H_2-SCR. Reaction conditions: NO = 1000 ppm, H_2 = 5000 ppm, O_2 = 6% with helium as balance, GHSV = 80 000 h^{-1}.

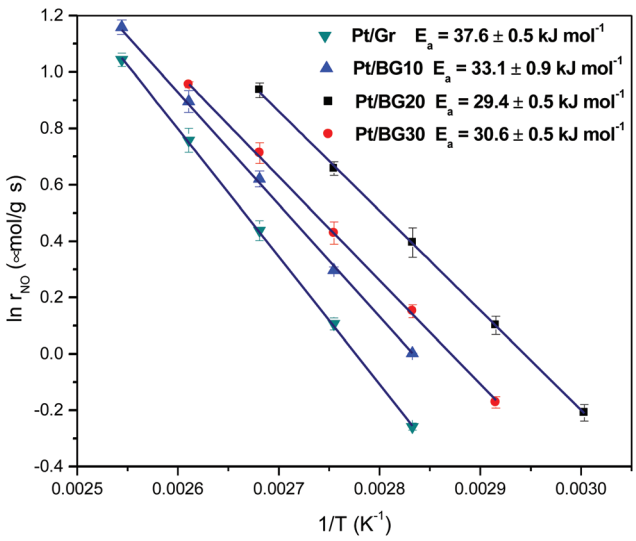

Fig. 8 Arrhenius plots of H_2-SCR over different catalysts.

Table 4 Comparison of different Pt catalysts for H_2-SCR reaction

Catalyst	Reaction conditions[a]	NO conversion	N_2 selectivity	Ref.
0.5%Pt-2%WO_3/TiO_2	0.25% NO, 1% H_2, 5% O_2, GHSV 53 000 h^{-1}, 150 °C	88%	80%	24
1%Pt/TiO_2–ZrO_2	800 ppm NO, 2800 ppm H_2, 10% O_2, W/F = 0.24 $sgcm^{-3}$, 90 °C	89%	53%	28
0.1%Pt/Pt/MgO–CeO_2	0.25% NO, 1% H_2, 5% O_2, GHSV = 80 000 h^{-1}, 150 °C	95%	75%	29
0.8%Pt/ZSM-5	1000 ppm NO, 5000 ppm H_2, 6.7% O_2, GHSV 78 000 h^{-1}, 100 °C	96%	70%	34
0.1%Pt-1%W/HZSM-5	910 ppm NO, 90 ppm NO_2, 5000 ppm H_2, 10% O_2, GHSV = 36 000 h^{-1}, 110 °C	91.1%	80%	35
1%Pt/Ti-MCM-41	1000 ppm NO, 5000 ppm H_2, 6.7% O_2, GHSV 80 000 h^{-1}, 140 °C	89%	79%	41
1%Pt/B-graphene	1000 ppm NO, 5000 ppm H_2, 6% O_2, GHSV 80 000 h^{-1}, 105 °C	94.7%	90.3%	This work

[a] Adapted as the optimal performance was observed.

O_{ad} and increased selectivity towards N_2 production.[74] NO dissociation is considered as the key step to produce adsorbed N atoms, and the subsequent formation of N_2.[3] The extra NO adsorption sites introduced by boron doping improved the N_2 selectivity by the H-assisted dissociative adsorption of NO.[75] The NO adsorbed on B sites would react with the spillover hydrogen to form N–O–H because the energy needed for the N–O bond dissociation was higher than that of N–O–H dissociation.[76] N–O–H further dissociated into N_{ad} and OH_{ad} and eventually formed N_2, leading to a higher selectivity on boron-doped catalysts. Another benefit from boron doping is the formation of acidic sites due to the electron donation from boron to carbon, which could facilitate NH_4^+ storage to enhance selective N_2 formation by the well-established NH_3-SCR mechanism.[17,33,34] All of the above three advantages originated from doped-boron would consume NO to produce N_2 only, which led to the improved overall selectivity to N_2 in H_2-SCR. Furthermore, it is worth mentioning that the reaction performance (including both activity and selectivity) of the Pt/BG catalyst for H_2-SCR is comparable to those of the reported Pt catalysts (Table 4), indicating that it has great potential in the future.

Based on the above characterization and reaction results, one probable bifunctional catalytic mechanism (Fig. 9) was proposed to illustrate the promotion effect of boron doping for H_2-SCR in the presence of excess oxygen. There are two types of adsorption sites for NO on Pt/BG catalyst surface, metallic Pt and doped boron. Hydrogen only adsorbed on the Pt sites with spillover. The superior activity can be attributed to the higher dispersion of Pt, more metallic Pt, and extra active sites for NO adsorption. The improved selectivity to N_2 was attributed to more metallic Pt formation, H-assisted dissociative adsorption of NO, and increased catalyst acidity, all of which were from boron doping.

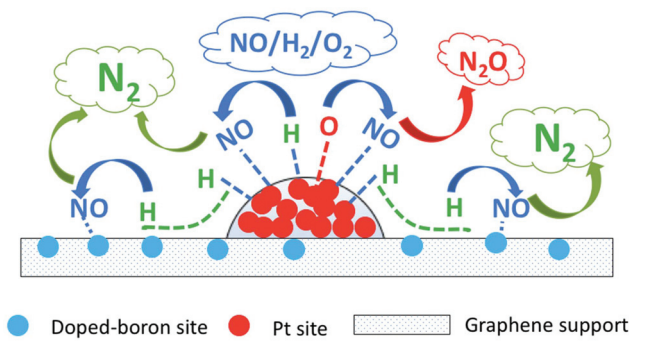

Fig. 9 Proposed bifunctional catalytic mechanism of H_2-SCR over Pt/BG catalyst in the presence of excess oxygen.

4. Conclusion

We demonstrated a strategy to design and prepare a superior catalyst system for H_2-SCR. The designed Pt/boron-doped graphene catalysts were prepared by a facile hydrothermal method. Boron doping into layered graphene was performed by replacing both carbon and oxygen atoms in the graphene oxide matrix, which was confirmed by ICP, XPS, and TPD. The doped-boron played multi-roles to affect both the structure and chemisorption ability of Pt/BG catalysts: (1) enhancing Pt dispersion due to the increased Pt nucleation rate over doped-boron; (2) facilitating hydrogen spillover by decreasing the Pt nanoparticle size; (3) promoting more metallic Pt formation by donating electrons from boron to Pt; (4) increasing H_2 adsorption by increasing Pt dispersion; and (5) improving NO adsorption by increasing Pt dispersion and providing extra foreign active sites. The reaction performance of the optimal Pt/BG for H_2-SCR (conversion 94.7%, selectivity 90.3%, activation energy 29.4 ± 0.5 kJ mol^{-1}, and TOF 0.092 s^{-1}) was greatly promoted due to the above-mentioned beneficial effects from boron doping. Its comparable performance with the reported work indicates its great potential applications in the future. This strategy definitely paves the way to modify the structure and tune the chemisorption ability of graphene-based catalysts, and provides novel insights for designing high performance catalysts.

Conflicts of interest

There are no conflicts to declare.

Acknowledgements

This work was supported by an ACS-PRF 53582-ND10.

References

1 M. Shelef, J. H. Jones, J. T. Kummer, K. Otto and E. E. Weaver, *Environ. Sci. Technol.*, 1971, **5**, 790–798.
2 R. Burch, A. A. Shestov and J. A. Sullivan, *J. Catal.*, 1999, **186**, 353–361.
3 Z. Liu, J. Li and S. I. Woo, *Energy Environ. Sci.*, 2012, **5**, 8799.
4 B. Frank, G. Emig and A. Renken, *Appl. Catal., B*, 1998, **19**, 45–57.
5 C. Xu, W. Sun, L. Cao and J. Yang, *Chem. Eng. J.*, 2016, **283**, 1137–1144.
6 L. Wang, C. Yin and R. T. Yang, *Appl. Catal., A*, 2016, **514**, 35–42.
7 F. Bin, C. Song, G. Lv, J. Song, S. Wu and X. Li, *Appl. Catal., B*, 2014, **150–151**, 532–543.
8 S. Cai, J. Liu, K. Zha, H. Li, L. Shi and D. Zhang, *Nanoscale*, 2017, **9**, 5648–5657.
9 S. Cai, H. Hu, H. Li, L. Shi and D. Zhang, *Nanoscale*, 2016, **8**, 3588–3598.
10 M. Qiu, S. Zhan, H. Yu, D. Zhu and S. Wang, *Nanoscale*, 2015, **7**, 2568–2577.
11 L. Huang, X. Zhao, L. Zhang, L. Shi, J. Zhang and D. Zhang, *Nanoscale*, 2015, **7**, 2743–2749.
12 S. Cai, D. Zhang, L. Shi, J. Xu, L. Zhang, L. Huang, H. Li and J. Zhang, *Nanoscale*, 2014, **6**, 7346–7353.
13 D. Zhang, L. Zhang, L. Shi, C. Fang, H. Li, R. Gao, L. Huang and J. Zhang, *Nanoscale*, 2013, **5**, 1127–1136.
14 P. M. More, D. L. Nguyen, P. Granger, C. Dujardin, M. K. Dongare and S. B. Umbarkar, *Appl. Catal., B*, 2015, **174–175**, 145–156.
15 P. S. Kim, M. K. Kim, B. K. Cho, I. S. Nam and S. H. Oh, *J. Catal.*, 2013, **301**, 65–76.
16 T. Nanba, C. Kohno, S. Masukawa, J. Uchisawa, N. Nakayama and A. Obuchi, *Appl. Catal., B*, 2003, **46**, 353–364.
17 H. Hamada and M. Haneda, *Appl. Catal., A*, 2012, **421–422**, 1–13.
18 L. Valanidou, C. Theologides, A. A. Zorpas, P. G. Savva and C. N. Costa, *Appl. Catal., B*, 2011, **107**, 164–176.
19 L. Wang, H. Chen, M. H. Yuan, S. Rivillon, E. H. Klingenberg, J. X. Li and R. T. Yang, *Appl. Catal., B*, 2014, **152–153**, 162–171.
20 G. Qi, R. T. Yang and F. C. Rinaldi, *J. Catal.*, 2006, **237**, 381–392.
21 Q. Yu, M. Richter, F. Kong, L. Li, G. Wu and N. Guan, *Catal. Today*, 2010, **158**, 452–458.
22 K. Polychronopoulou and A. M. Efstathiou, *Recent Pat. Mater. Sci.*, 2012, **5**, 87–104.
23 P. G. Savva and C. N. Costa, *Catal. Rev.: Sci. Eng.*, 2011, **53**, 91–151.
24 Z. Liu, Y. Lu, L. Yuan, L. Ma, L. Zheng, J. Zhang and T. Hu, *Appl. Catal., B*, 2016, **188**, 189–197.
25 R. Burch and M. D. Coleman, *J. Catal.*, 2002, **208**, 435–447.
26 L. Yuan, X. Zheng, K. Duan, H. Hu, J. Wang, S. I. Woo and Z. Liu, *Front. Environ. Sci. Eng.*, 2013, **7**, 457–463.
27 R. Burch, A. A. Shestov and J. A. Sullivan, *J. Catal.*, 1999, **188**, 69–82.
28 M. Machida, S. Ikeda, D. Kurogi and T. Kijima, *Appl. Catal., B*, 2001, **35**, 107–116.
29 C. N. Costa and A. M. Efstathiou, *Appl. Catal., B*, 2007, **72**, 240–252.
30 J. Lin, B. Qiao, N. Li, L. Li, X. Sun, J. Liu, X. Wang and T. Zhang, *Chem. Commun.*, 2015, **51**, 7911–7914.
31 S. Yang, X. Wang, W. Chu, Z. Song and S. Zhao, *Appl. Catal., B*, 2011, **107**, 380–385.
32 W. Sun, K. Qiao, J.-y. Liu, L.-m. Cao, X.-q. Gong and J. Yang, *ACS Comb. Sci.*, 2016, **18**, 195–202.
33 A. Satsuma, M. Hashimoto, J. Shibata, H. Yoshida and T. Hattori, *Chem. Commun.*, 2003, **9**, 1698–1699.
34 J. Shibata, M. Hashimoto, K. I. Shimizu, H. Yoshida, T. Hattori and A. Satsuma, *J. Phys. Chem. B*, 2004, **108**, 18327–18335.
35 X. Zhang, X. Wang, X. Zhao, Y. Xu, Y. Liu and Q. Yu, *Chem. Eng. J.*, 2015, **260**, 419–426.
36 Q. Yu, M. Richter, L. Li, F. Kong, G. Wu and N. Guan, *Catal. Commun.*, 2010, **11**, 955–959.
37 M. Machida and T. Watanabe, *Appl. Catal., B*, 2004, **52**, 281–286.
38 C. N. Costa, P. G. Savva, C. Andronikou, P. S. Lambrou, K. Polychronopoulou, V. C. Belessi, V. N. Stathopoulos, P. J. Pomonis and A. M. Efstathiou, *J. Catal.*, 2002, **209**, 456–471.
39 C. N. Costa, V. N. Stathopoulos, V. C. Belessi and A. M. Efstathiou, *J. Catal.*, 2001, **197**, 350–364.
40 J. Y. Jeon, H. Y. Kim and S. I. Woo, *Appl. Catal., B*, 2003, **44**, 301–310.
41 L. Li, P. Wu, Q. Yu, G. Wu and N. Guan, *Appl. Catal., B*, 2010, **94**, 254–262.
42 M. Hu, K. S. Hui and K. N. Hui, *Chem. Eng. J.*, 2014, **254**, 237–244.
43 M. Hu, Z. Yao, K. N. Hui and K. S. Hui, *Chem. Eng. J.*, 2017, **308**, 710–718.
44 M. Hu, Z. Yao and X. Wang, *Ind. Eng. Chem. Res.*, 2017, **56**, 3477–3502.
45 X. Tang, C. Li, H. Yi, L. Wang, Q. Yu, F. Gao, X. Cui, C. Chu, J. Li and R. Zhang, *Chem. Eng. J.*, 2018, **333**, 467–476.
46 X. Lu, C. Song, C.-C. Chang, Y. Teng, Z. Tong and X. Tang, *Ind. Eng. Chem. Res.*, 2014, **53**, 11601–11610.
47 X. Lu, C. Song, S. Jia, Z. Tong, X. Tang and Y. Teng, *Chem. Eng. J.*, 2015, **260**, 776–784.
48 X. Xiao, Z. Sheng, L. Yang and F. Dong, *Catal. Sci. Technol.*, 2016, **6**, 1507–1514.
49 Y. Sun, C. Du, G. Han, Y. Qu, L. Du, Y. Wang, G. Chen, Y. Gao and G. Yin, *Electrochim. Acta*, 2016, **212**, 313–321.
50 M. Hu, Z. Yao and X. Wang, *AIMS Mater. Sci.*, 2017, **4**, 755–788.
51 X. Bo, M. Li, C. Han and L. Guo, *Electrochim. Acta*, 2013, **114**, 582–589.
52 E. Chigo-Anota, M. A. Alejandro, A. B. Hernandez, J. J. S. Torres and M. Castro, *RSC Adv.*, 2016, **6**, 20409–20421.

53 C. Ling and F. Mizuno, *Phys. Chem. Chem. Phys.*, 2014, **16**, 10419–10424.
54 Y. Liu, Y. Shen, L. Sun, J. Li, C. Liu, W. Ren, F. Li, L. Gao, J. Chen, F. Liu, Y. Sun, N. Tang, H. M. Cheng and Y. Du, *Nat. Commun.*, 2016, **7**, 10921.
55 Y. Sun, C. Du, M. An, L. Du, Q. Tan, C. Liu, Y. Gao and G. Yin, *J. Power Sources*, 2015, **300**, 245–253.
56 N. I. Kovtyukhova, P. J. Ollivier, B. R. Martin, T. E. Mallouk, S. A. Chizhik, E. V. Buzaneva and A. D. Gorchinskiy, *Chem. Mater.*, 1999, **11**, 771–778.
57 M. Hu and X. Wang, *Catal. Today*, 2016, **263**, 98–104.
58 S. Agnoli and M. Favaro, *J. Mater. Chem. A*, 2016, **4**, 5002–5025.
59 T. Ye, D. P. Durkin, M. Hu, X. Wang, N. A. Banek, M. J. Wagner and D. Shuai, *ACS Appl. Mater. Interfaces*, 2016, **8**, 17739–17744.
60 Y. Yang, J. Zhang, X. Wu, Y. Fu, H. Wu and S. Guo, *J. Mater. Chem. A*, 2014, **2**, 9111–9117.
61 D. Y. Usachov, A. V. Fedorov, A. E. Petukhov, O. Y. Vilkov, A. G. Rybkin, M. M. Otrokov, A. Arnau, E. V. Chulkov, L. V. Yashina, M. Farjam, V. K. Adamchuk, B. V. Senkovskiy, C. Laubschat and D. V. Vyalikh, *ACS Nano*, 2015, **9**, 7314–7322.
62 V. Thirumal, A. Pandurangan, R. Jayavel and R. Ilangovan, *Synth. Met.*, 2016, **220**, 524–532.
63 A. Kalijadis, J. Đorđević, T. Trtić-Petrović, M. Vukčević, M. Popović, V. Maksimović, Z. Rakočević and Z. Laušević, *Carbon*, 2015, **95**, 42–50.
64 X. Zeng, Z. Wang, N. Meng, D. T. McCarthy, A. Deletic, J.-h. Pan and X. Zhang, *Appl. Catal., B*, 2017, **202**, 33–41.
65 H. N. Yang and W. J. Kim, *Electrochim. Acta*, 2016, **209**, 430–439.
66 M. Begliarbekov, O. Sul, S. Kalliakos, E.-H. Yang and S. Strauf, *Appl. Phys. Lett.*, 2010, **97**, 031908.
67 D. Graf, F. Molitor, K. Ensslin, C. Stampfer, A. Jungen, C. Hierold and L. Wirtz, *Nano Lett.*, 2007, **7**, 238–242.
68 S. Yamakawa, K. Okazaki-Maeda, M. Kohyama and S. Hyodo, *J. Phys.: Conf. Ser.*, 2008, **100**, 072042.
69 Y. Zhou, K. Neyerlin, T. S. Olson, S. Pylypenko, J. Bult, H. N. Dinh, T. Gennett, Z. Shao and R. O'Hayre, *Energy Environ. Sci.*, 2010, **3**, 1437–1446.
70 N. R. Stuckert, L. Wang and R. T. Yang, *Langmuir*, 2010, **26**, 11963–11971.
71 J. Lu, Y. Zhou, X. Tian, X. Xu, H. Zhu, S. Zhang and T. Yuan, *Appl. Surf. Sci.*, 2014, **317**, 284–293.
72 S. Kawai, S. Saito, S. Osumi, S. Yamaguchi, A. S. Foster, P. Spijker and E. Meyer, *Nat. Commun.*, 2015, **6**, 8098.
73 R. Burch and M. D. Coleman, *Appl. Catal., B*, 1999, **23**, 115–121.
74 K. Yokota, M. Fukui and T. Tanaka, *Appl. Surf. Sci.*, 1997, **121**, 273–277.
75 E. Shustorovich and A. T. Bell, *Surf. Sci.*, 1993, **289**, 127–138.
76 W. C. Hecker and A. T. Bell, *J. Catal.*, 1985, **92**, 247–259.

